AIAA JOURNAL
Vol. 47, No. 6, June 2009

Experimental Investigation of Unstart in an Inlet/Isolator Model in Mach 5 Flow

J. L. Wagner,* K. B. Yuceil,† A. Valdivia,‡ N. T. Clemens,§ and D. S. Dolling¶
University of Texas at Austin, Austin, Texas 78712-1085

DOI: 10.2514/1.40966

The dynamics of unstart of a floor-mounted inlet/isolator model in a Mach 5 flow are investigated experimentally. The inlet section contains a 6-deg compression ramp, and the isolator is a rectangular straight duct that is 25.4-mm high by 50.8-mm wide by 242.3-mm long. Measurements made include 8-kHz schlieren imaging and simultaneous fast-response wall pressures along the length of the inlet/isolator. Unstart is initiated by deflecting a flap at the downstream end of the isolator. The shock system, induced by unstart, initially propagates upstream through the isolator at a velocity of about 35 m/s (in the laboratory frame of reference), then decelerates to about 20 m/s near the isolator entrance, and then accelerates to a velocity of about 74 m/s within the inlet. Throughout the isolator, unstart is seen to be strongly associated with boundary-layer separation. Once the inlet has unstarted, a high-amplitude oscillatory (periodic) unstarted flow ensues, for which the oscillation frequency is about 124 Hz. However, under some conditions, an 84-Hz oscillatory unstarted flow mode, with lower pressure fluctuations, is observed. Under other conditions, a nonoscillatory unstarted flow, with much lower pressure fluctuations, is observed.

Nomenclature

a = speed of sound
f = frequency
f^* = normalized frequency $= fL/a_0$
H_0 = inlet entrance height
h = isolator height
L = model length
M = Mach number
P = pressure
Re = Reynolds number
T = temperature
t = time
U = streamwise velocity
x = streamwise coordinate
y = wall-normal coordinate
δ = boundary-layer thickness
δ^* = displacement thickness
θ = momentum thickness
σ = standard deviation
ϕ = high-amplitude unstarted flow cycle time

Subscripts

m = mean
0 = stagnation
∞ = freestream condition

I. Introduction

SCRAMJET and ramjet propulsion are developing technologies for a future generation of hypersonic atmospheric and space vehicles. The dual-mode engine concept proposed by Curran and Stull [1] allows the engine to act in ramjet mode at lower supersonic flight Mach numbers and then transition to scramjet mode at higher supersonic to hypersonic flight Mach numbers. Since the dual-mode proposal in 1963, much work has gone into understanding the complex flowfields involved, improving the performance of such engines, and developing methods of practical implementation [2–16].

In the dual-mode engine, the precombustion compression components are the inlet and the isolator [2]. The isolator is a duct connecting the inlet to the combustor. An important performance measure for an inlet/isolator is its capability to provide an increase in static pressure before the combustor. Factors influencing the maximum static pressure gain in an inlet/isolator include the isolator length [4,7–11], isolator aspect ratio [13], isolator entrance flow profile [5,6], and geometry of the inlet [4]. In addition to providing compression, the isolator also serves to reduce the sensitivity of the inlet to combustor pressure perturbations [2–4].

In the ramjet mode of operation, a strong precombustion shock system forms in the isolator, resulting in subsonic combustor entrance flow [2,3]. The pressure rises in this shock system typically through a series of shocks known as a "shock train." Depending on the isolator entrance conditions, this can be either a normal shock train, containing a series of bifurcated normal shocks, or an oblique shock train which contains a series of crossing oblique shocks [3,7]. Normal shock trains occur for lower entrance Mach numbers of about 2–3, whereas oblique shock trains occur for higher entrance Mach numbers [3]. If the duct or isolator is sufficiently long, a mixing region containing further compression will follow a shock train. This shock train, in combination with the subsequent mixing region, has been referred to as a "pseudoshock" in the literature [7]. The maximum pressure rise in a pseudoshock is less than, but can be near, the value given by a single normal shock at the entrance Mach number [7]. Extensive work has been directed at investigating the characteristics of internal flows containing shock trains [7–9,11]. For example, the empirical correlations of Waltrup and Billig [8,9], have accurately matched wall-pressure distributions measured in the isolator in the dual-mode studies [10,11], highlighting their potential to be used as design tools.

The isolator also plays an important role in the scramjet mode of operation of the dual-mode engine [2]. As is often the case, heat addition to the supersonic combustor flow can result in an adverse pressure gradient which can lead to separation of the boundary

---

Presented as Paper 4352 at the 37th Fluid Dynamics Conference and Exhibit, Miami, FL, 25–28 June 2007; received 12 September 2008; revision received 27 January 2009; accepted for publication 28 January 2009.

*Graduate Research Assistant, Center for Aeromechanics Research, Department of Aerospace Engineering and Engineering Mechanics. Student Member AIAA.

†Visiting Professor, Center for Aeromechanics Research, Department of Aerospace Engineering and Engineering Mechanics. Member AIAA.

‡Graduate Research Assistant, Center for Aeromechanics Research, Department of Aerospace Engineering and Engineering Mechanics.

§Professor, Center for Aeromechanics Research, Department of Aerospace Engineering and Engineering Mechanics. Associate Fellow AIAA.

¶Professor, Center for Aeromechanics Research, Department of Aerospace Engineering and Engineering Mechanics. Fellow AIAA.

layers. This pressure disturbance propagates upstream and results in the formation of an oblique shock train (with a supersonic core flow) in the isolator [2].

Disturbances, such as those due to combustion, can lead to a transient process known as unstart [2,3]. When unstart occurs, the original inlet/isolator compression (shock) system is displaced upstream out of the inlet and it can eventually take the form of a detached bow shock [3]. The unstart process can be severe with high transient pressure loads, and it can lead to a loss of engine thrust [3]. In the ramjet mode of operation, a strong precombustion shock system exists within the isolator to slow the flow to subsonic speeds. If the combustion pressure rises to a value that cannot be matched by this shock system, the engine will unstart [2]. Combustion perturbations can also lead to unstart in the scramjet mode of operation in two ways: 1) too much heat addition can lead to the thermally choked (sonic) condition [2], and 2) heat addition can create excessive boundary-layer separation and hence increased blockage [2].

Unstart has been the subject of a number of experimental studies [17–21]. For example, Wieting [17] used a three-dimensional model scramjet and initiated unstart by inserting a cylindrical pin to create blockage. Peak pressures during unstart were seen to be up to 20 times the started values. It was found that the peak pressures could be conservatively estimated by the pressure that would be found behind a stationary normal shock. Propagation velocities of the unstart shock system, as calculated by pressure measurements, ranged from 10–27 m/s (in the lab frame of reference). In another study [18], unstart was investigated in a two-dimensional dual-mode model. The model could be pressurized to a maximum and eventually unstarted by raising a flap in the model's nozzle section. In addition, the inlet cowl could be adjusted to vary the inlet contraction ratio (i.e., the ratio of the cross-sectional area of the captured stream tube to the inlet throat area). Higher inlet contraction ratios were seen to result in what were defined as "hard unstarts," whereas lower inlet contraction ratios resulted in "soft unstarts." A hard unstart was defined to be that which resulted in an unstarted flow with much "flatter" (lower) mean pressures in the isolator and combustor sections compared to the maximum pressures before unstart occurred. Also, some hard unstarts were seen to result in oscillatory (periodic) unstarted flows with frequencies of about 300 Hz. Soft unstarts were defined as those which occurred gradually while maintaining a pressure distribution more similar to that before unstart. Unstart propagation velocities were reported to range from 55 to 70 m/s. Shimura et al. [19] induced unstart in a three-dimensional combusting scramjet model by increasing the mass flow rate of hydrogen fuel. For fuel flow rates near that which caused unstart, distinct pressure spikes were observed upstream of the isolator entrance. It was therefore suggested that unstart could be avoided and controlled by monitoring this pressure and reducing the fuel rate accordingly. Hawkins and Marquart [20] used a two-dimensional supersonic/hypersonic inlet and initiated unstart by raising flaps at the rear of the model. Shadowgraph imaging showed the inlet flow to be highly separated after unstart. Similar to Rodi et al. [18], oscillatory unstarted flows were observed with frequencies of 150–180 Hz. A more fundamental experimental study by O'Byrne et al. [21] focused on the thermal choking process in a model scramjet. The model consisted of only an isolator and fuel injector. Heat addition due to supersonic combustion was seen to lead to the formation of a normal shock that subsequently propagated upstream. The flow behind this normal shock was seen to have a Mach number near unity and it was suggested that heat addition forced the shock upstream.

Computational fluid dynamics simulations have also been used to study unstart [22–25]. Sato and Kaji [22] proposed that the process of unstart occurs as the "boundary-layer flow spreads and pushes out the main flow" of the engine inlet. Neaves et al. [23] simulated unstart of the model dual-mode engine studied by Emami et al. [4] and made some interesting observations. In the experiment and the simulation, unstart was induced with the raising of a flap in the nozzle section. Before unstart, the model was pressurized, resulting in the formation of a shock system near the isolator exit. During unstart, the unstart system seemed to stop its upstream propagation momentarily in the isolator while the reflected oblique shocks due to the inlet cowl became stronger and induced separation. Propagation of the unstart system then continued with increasing separation. Three-dimensional computations by McDaniel and Edwards [25] were made to investigate unstart in the model scramjet used in the experiments of Masuya et al. [15]. The simulations gave much physical insight into the possible cause of unstart in the experiments. Supersonic combustion was seen to result in an increase in the strength of the fuel injector recompression shocks, which caused boundary-layer separation. Hydrogen was then entrained into the hot portions of the separated flow resulting in ignition and massive shock-induced separation. This blockage was seen to lead to unstart before the thermally choked condition was reached. At the end of the unstart process, the isolator flow was seen to be highly three-dimensional. For example, flow in the spanwise center plane was seen to be supersonic, whereas flow near the sidewalls was highly reversed with a peak velocity of 420 m/s.

The preceding discussion shows that, although substantial work has been aimed at understanding unstart, much remains unknown about unstart dynamics. Lack of understanding of the unstart process is particularly critical if new strategies for controlling it are to be developed. The current paper describes the results of an experimental study of unstart and unstarted flows in an inlet/isolator model that was mounted on the floor of a Mach 5 wind tunnel. The model, which is designed with a simple compression surface and a straight rectangular isolator, represents a simplified form of a dual-mode scramjet inlet/isolator. Unstart was initiated by deflecting a flap located at the exit of the isolator. The unstart process and resulting unstarted flow were studied by using simultaneous high-speed schlieren imaging and wall-pressure measurements. The data were used to characterize the flow structure during unstart and to determine the relevant time scales involved in unstart and unstarted flows.

II. Experimental Setup

A. Facility and Test Model

The experimental data were taken in the Mach 5 blowdown wind tunnel at the University of Texas at Austin. The wind-tunnel air was supplied by storage tanks with a volume of 4 m^3 (140 ft^3) at a pressure of 17.6 MPa (2550 psia). Tests were conducted at plenum temperature of $T_0 = 333 \pm 3$ K(600 ± 5°R) and freestream pressure of $P_\infty = 5.38$ kPa (0.78 psia). The freestream Mach number, velocity, and unit Reynolds number were 4.9, 740 m/s (2460 ft/s), and $49.5 \times 10^6\ \mathrm{m}^{-1}$ ($15.1 \times 10^6\ \mathrm{ft}^{-1}$), respectively. The constant area test section was 15.2-cm (6-in.) wide by 17.8-cm (7-in.) tall and had a length of 76.2 cm (30 in.). Fused silica windows 38.1-cm (15-in.) long and 5.1-cm (2-in.) tall were placed in the test section side walls for optical access.

The inlet/isolator model was mounted on the floor of the test section as shown in Fig. 1. Figures 1a and 1b show schematics of the model with one sidewall removed with the flap fully down and the flap raised to an angle great enough to induce unstart. Figure 1c shows a photograph of the model. The coordinate system is in nondimensional units normalized by the isolator height h. The inlet portion of the model consisted of a 6-deg compression ramp with aft-swept sidewalls. The sidewall sweep angle was 53.5 deg with respect to the wall-normal y axis. The inlet entrance height H_0 was 34.9 mm (1.375 in.) and the throat height at the entrance of the isolator section was 25.4 mm (1.00 in.). The constant area isolator and inlet were 242.3-mm (9.54-in.) and 90.7-mm (3.57-in.) long, respectively. The inner width of the model was 50.8 mm (2.00 in.) giving an inlet entrance aspect ratio of 1.45 and an isolator aspect ratio of 2. The model was a bolted assembly of four pieces. The upstream piece, made out of aluminum, contained the ramp and the isolator throat. A small portion of the isolator 11.2-mm (0.44-in.) long was also contained within the aluminum upstream piece. The rest of the isolator was formed from an aluminum ceiling and two acrylic sidewalls to allow optical access. This resulted in a streamwise length of 231.1 mm (9.06 in.) where the flow within the

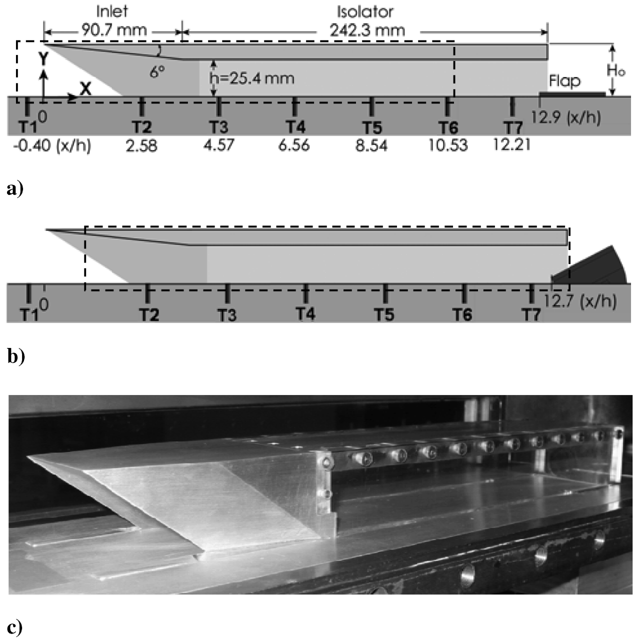

Fig. 1 Schematics of the inlet/isolator model instrumented for simultaneous optical and pressure measurements: a) with flap fully down, b) with flap up at the unstart angle of 28 deg, and c) photograph of the inlet/isolator model mounted on the wind-tunnel floor.

isolator could be visualized. The thickness of the all three isolator pieces was 9.5 mm (0.375 in.).

A mechanical flap was raised to simulate the combustor pressure rise. As shown in Fig. 1a, in the fully down position, the top of the flap was 3.2 mm (0.125 in.) above the isolator floor. In the fully down position, the leading edge of the flap was at the streamwise coordinate of $x/h = 12.9$. The model was seen to unstart when the flap was raised to an angle of 28 deg. The uncertainty in determining the unstart angle was estimated to be ±3 deg. The flap was hinged to the wind-tunnel floor at a location below $y = 0$. As shown in Fig. 1b, this resulted in the leading edge of the flap moving upstream to $x/h = 12.7$ at the unstart angle. The drive system was able to move the flap from its fully down position to the unstart angle in about 140 ms.

Owing to the floor-mounted configuration, the inlet ingested the test section floor boundary layer, which was turbulent and quite thick as compared to the inlet height. The floor boundary layer had the following properties: 99% thickness $\delta = 19.3$ mm (0.76 in.), displacement thickness $\delta^* = 9.1$ mm (0.35 in.), momentum thickness $\theta = 0.75$ mm (0.03 in.), and Reynolds number based on momentum thickness $Re_\theta = 39,000$. The boundary layers on the other walls of the inlet developed naturally.

B. High-Speed Schlieren, Fast-Response Pressure Measurement and Motor Drive Control Systems

A schematic of the measurement system setup is shown in Fig. 2. A rack-and-pinion system driven by a servo motor (Oriental Motor BX series) was used to control the flap. The servo motor was driven by a computer running a LabVIEW (National Instruments) control program. A data acquisition card (National Instruments PCI-6221) in the computer was used to output the motor control signals. The high-speed schlieren system operated at a framing rate of 8 kHz and consisted of a high-brightness pulsed light-emitting diode (LED) light source (ISSI, Inc.), two 318-mm (12.5-in.) diameter mirrors with focal lengths of 152 mm (72 in.), and a high-framing rate complementary metal oxide semiconductor camera (Photron FastCam-Ultima APX) fitted with a 105-mm $f/2.8$ lens (Nikon AF Micro-Nikkor). The camera was shuttered to 10 μs and the image resolution was 1024×128 pixels. A row of seven fast-response pressure transducers were flush mounted in a row near the spanwise centerline of the inlet/isolator model. The transducers had an effective frequency response of 50 kHz. The transducer locations are labeled T1–T7 on the schematic of Fig. 1. T1 (Kulite XCQ-062-15A) had a range of 0–100 kPa (0–15 psia) and T2–T7 (Kulite XCQ-062-50A) had ranges of 0–350 kPa (0–50 psia). T7 was on the spanwise centerline of the model, whereas transducers 1–6 were shifted slightly off center by 4.1 mm (0.16 in.) in the starboard direction to accommodate a laser-exit window (to be used in future experiments). The transducer signals were each sent through a wideband differential dc amplifier (Dynamics model 7525) and then low-pass filtered at 50 kHz using an active filter (DL model 4302 or Ithaco

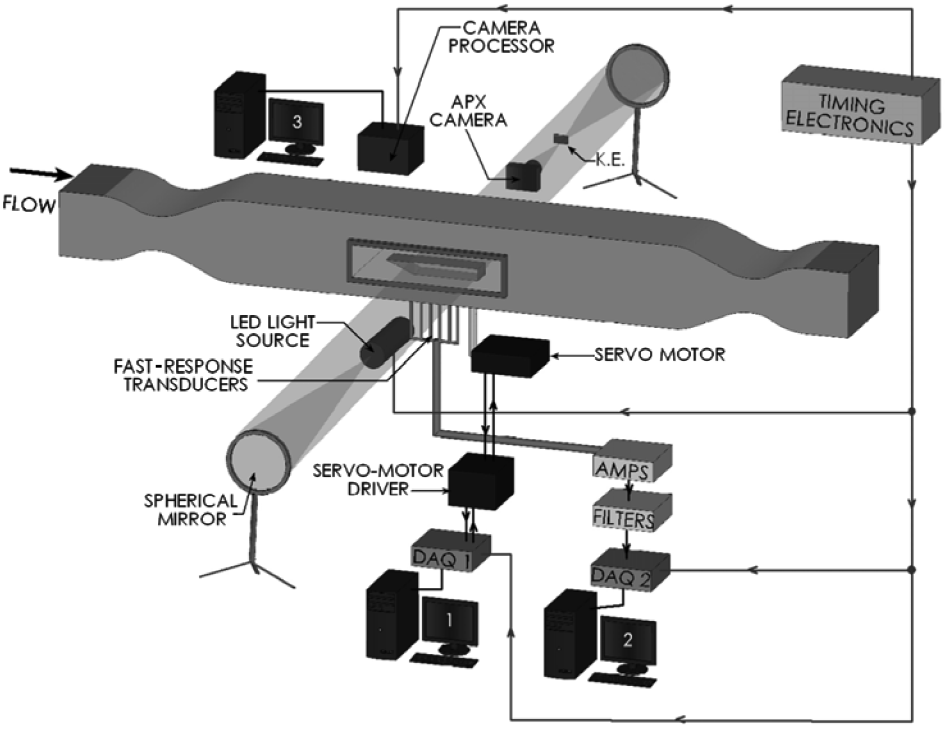

Fig. 2 Schematic of the model in the Mach 5 wind tunnel with schlieren imaging and instantaneous pressure measurements setup.

S30). The filtered signals were digitized at a rate of 192 kHz with 2 A/D cards (National Instruments DAQ PCI-6110E) mounted in a personal computer. The A/D cards were controlled by a Labview code developed inhouse. The total noise band of the electronics added an uncertainty of about ±0.55 kPa (±0.08 psi) to instantaneous pressure values reported herein. The transducers were calibrated using least-squares linear regression fits and a factory-calibrated precision dial gauge (Heise model CMM). All pressure values used to generate the calibration lines fell within 1% of the corresponding linear fit values. To test the repeatability of the pressure measurements, mean inlet/isolator pressure distributions with the flap fully down were acquired on three different runs of the wind tunnel with the same flow conditions. In addition, linear fits corresponding to two different calibrations were applied to these three raw data sets to quantify the repeatability of the calibration. This resulted in a sample of six different mean values for the same flow conditions corresponding to each transducer location. The rms of the six mean values was then calculated for each transducer location. The average rms was 0.3 kPa (0.04 psi). Therefore, the uncertainty of mean pressure values reported herein is estimated to be ±1% or 0.3 kPa (±0.04 psi), whichever is greater. The pressure data and imaging systems were synchronized in such a way that two pressure measurements were recorded during the 10 μs exposure time of each schlieren image. The timing electronics, which were used to synchronize the schlieren imaging, pressure measurement, and motor drive control systems, consisted of three pulse/delay generators (Stanford Research Systems DG535) and an inhouse-built divide-by circuit.

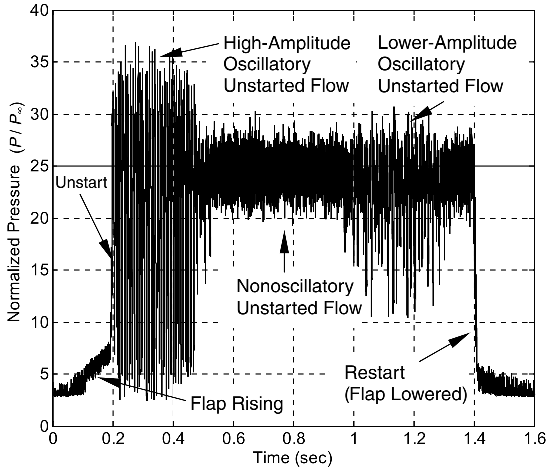

Fig. 3 Pressure time history corresponding to inlet unstart, unstarted flows, and restart processes obtained at T7.

C. Schlieren Imaging Fields of View

The entire length of the inlet/isolator model was 333 mm (13.1 in.), but the maximum schlieren field of view obtainable was 318 mm (12.5 in.) owing to the size of the schlieren mirrors. Therefore, to image the entire flowfield, including about 25 mm upstream of the inlet, two overlapping fields of view were used. The two fields of view are referred to in this paper as the upstream view and downstream view. As shown with the dashed-line rectangle in Fig. 1a, the upstream view extended from outside the inlet at $x/h = -0.7$ to inside the isolator at $x/h = 10.8$. As shown in Fig. 1b, the downstream view imaged the entire isolator section where the flow was visible. These two fields of view were not acquired simultaneously but on different runs of the wind tunnel.

III. Results

A. T7 Pressure Time History During Unstart/Restart

Figure 3 shows a time history of the wall pressure measured by transducer number 7 (T7 in Fig. 1) during a rather complex sequence of flap positions. During this sequence, the flap began in the fully down (undeflected) position and was then raised to about 28 deg to initiate unstart. Once the flow was unstarted, the flap was then lowered slightly, raised, and then lowered again. The purpose of performing this complex sequence is to show the differing flow behaviors that can be achieved with different flap positions. The time record is 2-s long and includes regions with different distinct pressure signatures. The specific sequence is as follows. From 0 to about 0.05 s, the downstream flap (throttle) is in the fully down position and the inlet/isolator is started with supersonic flow throughout. After 0.05 s, the computer instructs the flap to rise and at about 0.19 s, the pressure rises rapidly as unstart begins. From 0.20 to 0.45 s, high-amplitude pressure oscillations are seen. This region is termed high-amplitude oscillatory unstarted flow. At about 0.5 s, the flap is lowered slightly such that the flow is still unstarted but the pressure fluctuations are less intense. This region of unstarted flow is seen to have nonperiodic pressure fluctuations and is termed nonoscillatory unstarted flow. At about 0.95 s, the flap is again raised, which leads to an increase in the unstarted flow pressure fluctuations, but not to values as high as observed after the initial unstart pressure rise. These pressure fluctuations are also seen to exhibit strong periodicity. This region of unstarted flow is termed lower-amplitude oscillatory unstarted flow. Finally, the fall in pressure at about 1.4 s corresponds to a lowering of the flap and the subsequent restart of the inlet/isolator.

B. Fully Supersonic Started Flow

Figure 4 shows upstream- and downstream-view schlieren images for the started fully supersonic inlet/isolator. White lines mark the floor, 6-deg compression ramp, and the isolator ceiling. The inlet section, with its swept sidewalls, are seen in shadow because they are

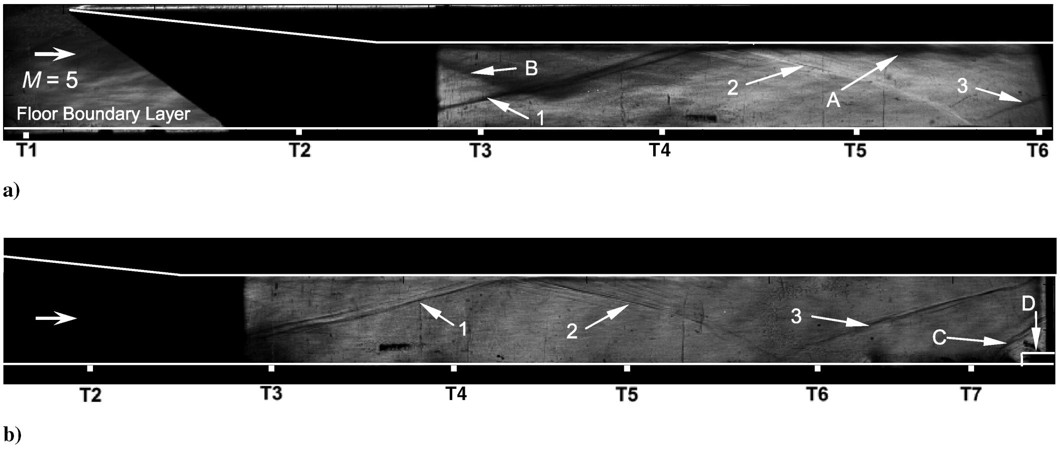

Fig. 4 Schlieren images of started flow: a) upstream view obtained with a horizontal knife edge, and b) downstream view obtained with a vertical knife edge.

made of aluminum. The upstream view (Fig. 4a) was obtained using a horizontal knife edge to reveal vertical density gradients such as those due to boundary layers. As labeled, the thick ($\delta = 19.3$ mm) floor boundary layer entering the inlet is visualized as a bright region, whereas the thin ceiling boundary layer is seen as a dark region (arrow A). The initial oblique shock from the inlet ramp is visually blocked by the inlet's aluminum sidewalls, but the first reflected shock is seen near the isolator entrance as a dark line (arrow 1). The first reflected shock impinges on the isolator ceiling, which results in an increase in boundary-layer thickness downstream of the impingement point. The subsequent reflected shock is seen as a bright line (arrow 2), which then reflects again from the isolator floor (arrow 3). The expansion fan originating at the inlet shoulder can also be seen as a dark region that enters the field of view in the upper left-hand portion of the isolator (arrow B). Figure 4b shows a downstream-view schlieren image of the started flow. The image was acquired using a vertical knife edge to highlight horizontal density gradients. All three reflected shocks are captured in this field of view (arrows 1–3). The final reflected shock intersects the isolator ceiling near the exit of the model. A detached shock (arrow C) is seen to form just upstream of the flap (arrow D).

The mean P_m and rms σ pressure distributions are shown in Fig. 5. All pressures reported herein are normalized by that measured at T1, which is assumed to equal the freestream pressure P_∞. The pressure at T1 was measured to be 5.38 kPa (0.78 psia). Figure 5a shows that the mean pressure remains nearly constant from T1 ($x/h = -0.40$) upstream of the inlet to T2 ($x/h = 2.58$) within the inlet portion of the model. An additional pressure increase is seen at T3 ($x/h = 4.57$). At T3, the flow has been processed by the 6-deg ramp shock as well as the first reflected oblique shock. Using inviscid oblique shock theory, the pressure ratio of the freestream to that processed by two oblique shocks with flow deflection angles of 6 deg is computed to be 3.7. The pressure ratio P_3/P_1 is measured to be 3.6, which is in good agreement. Moving downstream, the pressure then decreases across T4 ($x/h = 6.56$) and T5 ($x/h = 8.54$) as the flow passes through reflections of the inlet shoulder expansion fan. The maximum mean pressure for the started case occurs at T6 ($x/h = 10.53$) just behind the second reflected oblique shock. Just upstream of the flap shock, the pressure at T7 ($x/h = 12.21$) is slightly lower than that at T6, which is most likely a result of the flow passing through additional reflected expansions. The rms pressure distribution shows T3, T6, and T7 to have the highest fluctuations. Pressure transducers T3 and T6 are just downstream of impinging shocks, whereas T7 is just upstream of the flap shock. It therefore appears that shock wave/turbulent boundary-layer interactions are responsible for the increased pressure fluctuations.

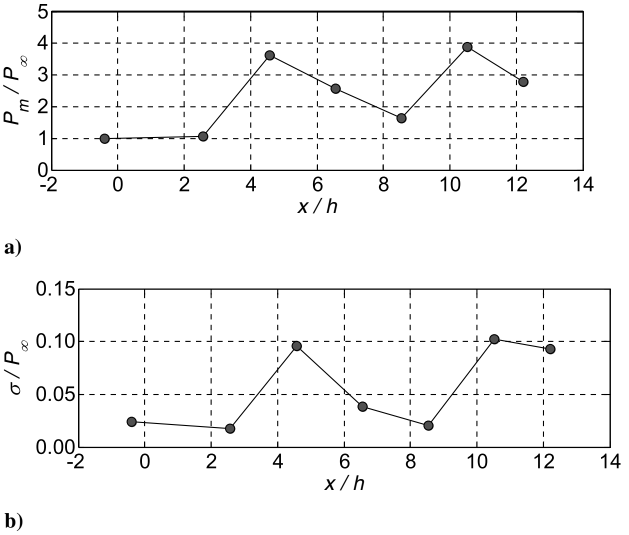

b)

Fig. 5 Fully supersonic started flow: a) mean pressure distribution, and b) pressure standard deviation distribution.

C. Initiation of Unstart

Figure 6 shows the pressure time history at pressure transducer T7 with a smaller time window than used in Fig. 3, which emphasizes the beginning of the unstart event. During the unstart process, the pressure at T7 rises by about 500%, from 0.19 to 0.2 s. Similar pressure increases were observed in all other unstart events examined. Figure 7 shows a schlieren image (emphasizing vertical gradients) for the case where the flap (arrow A) has been raised to an angle of about 28 deg to induce unstart. Again, the shape of the flap is a result of the 3.2-mm step as well as the upstream displacement of the flap's leading edge that occurs when it is raised. The detached flap shock (arrow B) and third reflected shock (arrow C) are impinging in close proximity to one another on the isolator ceiling near the exit. Near the impingement point of these shocks, the upper boundary layer of the isolator has separated, forming a separation shock (arrow D). Although not visible with this schlieren image, there are also interactions between these shocks and the isolator sidewall boundary layers (these are termed glancing shock interactions). The semi-empirical correlation by Korkegi [26] suggests that it is very likely that the sidewall boundary layers have also separated due to interactions with the flap shock. These separated flows are expected to lead to large viscous blockage effects that combine with the blockage of the flap. As will be discussed later, unstart seems to be associated with the presence of this severe separation at the downstream end of the isolator. Owing to these strong shock/boundary-layer interactions, it was not possible to set up a strong stable shock system, analogous to that found in a ramjet isolator, by raising the flap. This unstart initiation mechanism is similar to the cause of unstart seen in the computational study of McDaniel and Edwards [25], in which sidewall boundary-layer separation due to combustion was seen to initiate unstart of a model scramjet.

The ceiling separation shock (arrow D) in combination with the flap shock (arrow B) form what we term the unstart shock system. As will be shown, the unstart process involves the upstream propagation of the unstart shock system through the model which results in significant changes to the flow structure.

D. Unstart Time-Scales vs Flap Rise-Time

The effect of flap rise time on unstart was investigated. The fast-response pressure measurements were used to calculate the time-scales involved in the unstart process. As the unstart shock system crossed over T6 to T1, a clear rise in pressure was recognized, which allowed the times that the unstart shock system spent between transducers to be determined. The crossing time was defined to be the time that corresponded to the pressure at a given transducer becoming greater than a threshold value. The threshold pressure was chosen for each transducer to be just above those caused by preunstart pressure fluctuations. The times for 10 different unstart

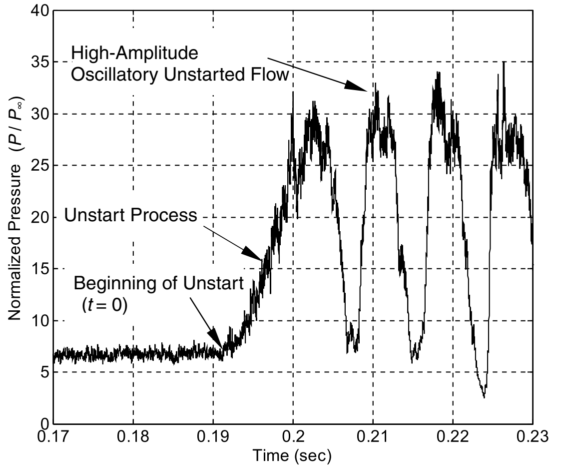

Fig. 6 T7 pressure time history of the unstart process followed by high-amplitude oscillatory unstarted flow cycles.

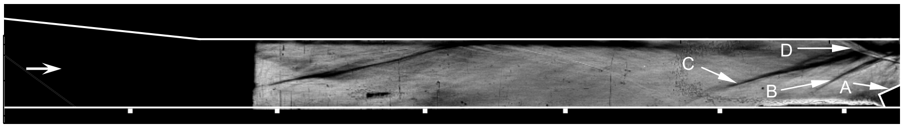

Fig. 7 Downstream-view schlieren image showing the flow just before the onset of unstart.

events are shown in Fig. 8a. For all of the unstart events shown in Fig. 8a, the flap was brought to a final angle of about 28 deg. The minimum achievable rise time (due to flap drive mechanical limitations) was about 140 ms. The "fast-flap" data correspond to unstart events induced during upward motion of the flap at the maximum possible flap speed (minimum flap rise time). The "slow-flap" data correspond to an unstart event induced during a flap rise time of about 530 ms. Obviously, neither of these times are nearly as short as flow transit times within the inlet and so the flow for both cases is probably quasi steady. High-speed schlieren imaging showed unstart began when the flap was near its final angle for both the fast-flap and slow-flap data of Fig. 8a. In some cases, the flap was brought to the final angle of about 28 deg and unstart did not occur during the rise time of the flap nor immediately thereafter. Rather, the model remained started and would then unstart at an unpredictable later time while the flap remained at its terminal angle. Two of these unstart events are shown in Fig. 8a and are termed natural unstarts. Collectively, the 10 unstart events of Fig. 8a do not show any discernible influence of flap speed on the time scales of the unstart process. Also, schlieren imaging did not show distinguishable differences in the flow structure of unstart that was initiated naturally or at the different flap speeds.

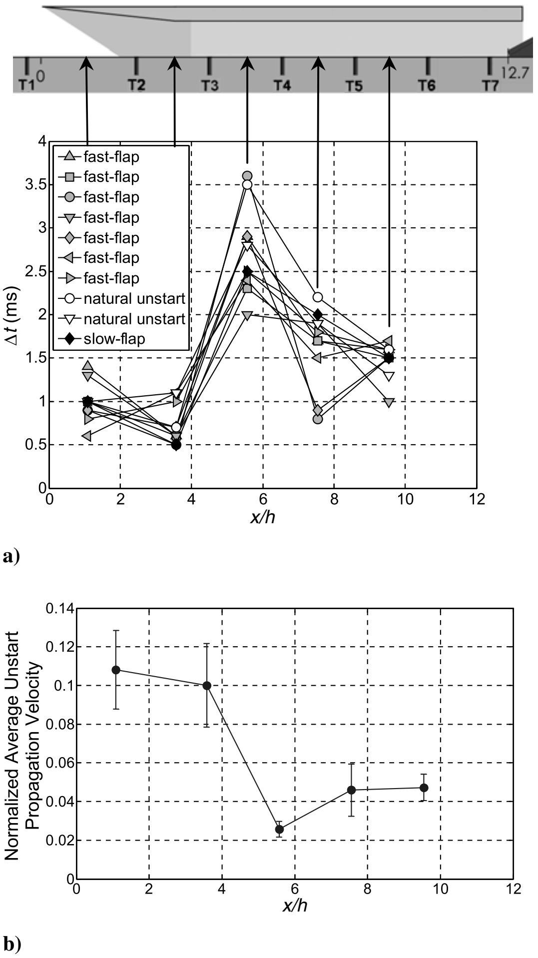

Fig. 8 Unstart time scales and velocities: a) unstart time scales for 10 runs (times spent between consecutive transducers), and b) normalized (by U_∞) average unstart shock system velocities based on the 10 runs.

E. Unstart Dynamics

To aid in the characterization of the unstart dynamics, the onset of unstart was defined by using either the downstream-view schlieren imaging or the pressure time history of T7. In this paper, $t = 0$ refers to the time at the onset of unstart. An example of a $t = 0$ schlieren image is shown in Fig. 9a ($t = 0$). Near the onset of unstart, the shock system created by the flap and final reflected shock (arrows A and C) was seen to go from relatively stationary to having significant upstream motion. The frame just before this upstream motion was observed was defined as the $t = 0$ of the unstart process. This definition of the onset of unstart is termed the schlieren-determined onset of unstart. Using this definition for a number of repeated runs, unstart onset could be determined with an uncertainty of ± 0.4 ms. As an alternative technique, the onset of unstart was determined by using the pressure time history of T7. As illustrated in Fig. 6, the estimated beginning of unstart is chosen to be the point in time where the pressure increases above the background fluctuations before unstart. This definition of the beginning of unstart is termed the pressure-determined onset of unstart. For this particular unstart event, it so happened that the time of the pressure-determined onset of unstart (0.1911 s) coincided closely with the schlieren-determined onset of unstart time (0.1913 s). However, for some unstart events, the rise in the pressure at T7 was less pronounced than seen in Fig. 6. This lack of a clear rise in pressure made it difficult to pick the onset of unstart from the T7 pressure time history alone. For the 10 unstart events of Fig. 8a, both the schlieren-determined and pressure-determined onset times of unstart were estimated. On average, the pressure-determined onset time was 1.0 ms earlier than the schlieren-determined onset time. The standard deviation of the difference between these times was 1.2 ms, which shows the two could differ significantly. In general, the schlieren-determined onset was found to be much more identifiable (and therefore reliable) than the pressure-determined onset of unstart. Therefore, the schlieren-determined onset of unstart is used in this paper wherever downstream-view imaging is available.

The total time for the model to unstart was determined by using the schlieren imaging and the T1 pressure time history. As explained earlier, when the unstart shock system reached T1 upstream of the inlet, a rise in pressure was observed. The inlet/isolator was defined to be unstarted at the time of this pressure rise. Based on the 10 unstart events of Fig. 8a, the average unstart total time is 8.2 ms (± 0.6 ms). The standard deviation, maximum, and minimum of the 10 unstart times are 0.7, 9.9, and 7.3 ms, respectively.

Upstream propagation velocities of the unstart shock system were computed using the times spent between transducers for the 10 unstart events of Fig. 8a. The velocities of the 10 unstart events were averaged to produce the velocity distribution shown in Fig. 8b. The velocities have been normalized by the freestream velocity of 740 m/s and are plotted at streamwise positions corresponding to the midpoints between consecutive transducers. The uncertainty ranges are based on 95% confidence intervals. The relatively large uncertainties in time (± 0.4 ms) associated with the schlieren-determined onset of unstart, combined with uncertainties in identifying the initial position of the unstart shock system, made it difficult to determine meaningful unstart propagation velocities downstream of T6. Therefore, only propagation velocities upstream of T6 are shown. Figure 8b shows the average propagation velocity of the unstart shock system to be about 0.047 U_∞ (35 m/s) in the middle portion of the isolator. The average velocity then slows to about 0.026 U_∞ (19 m/s) in the upstream portion of the isolator. The unstart shock system then accelerates upstream through the inlet. The average propagation velocity in the inlet (between T3 and T1) is 0.10 ± 0.01 U_∞ (74 ± 7 m/s) which is close to the maximum

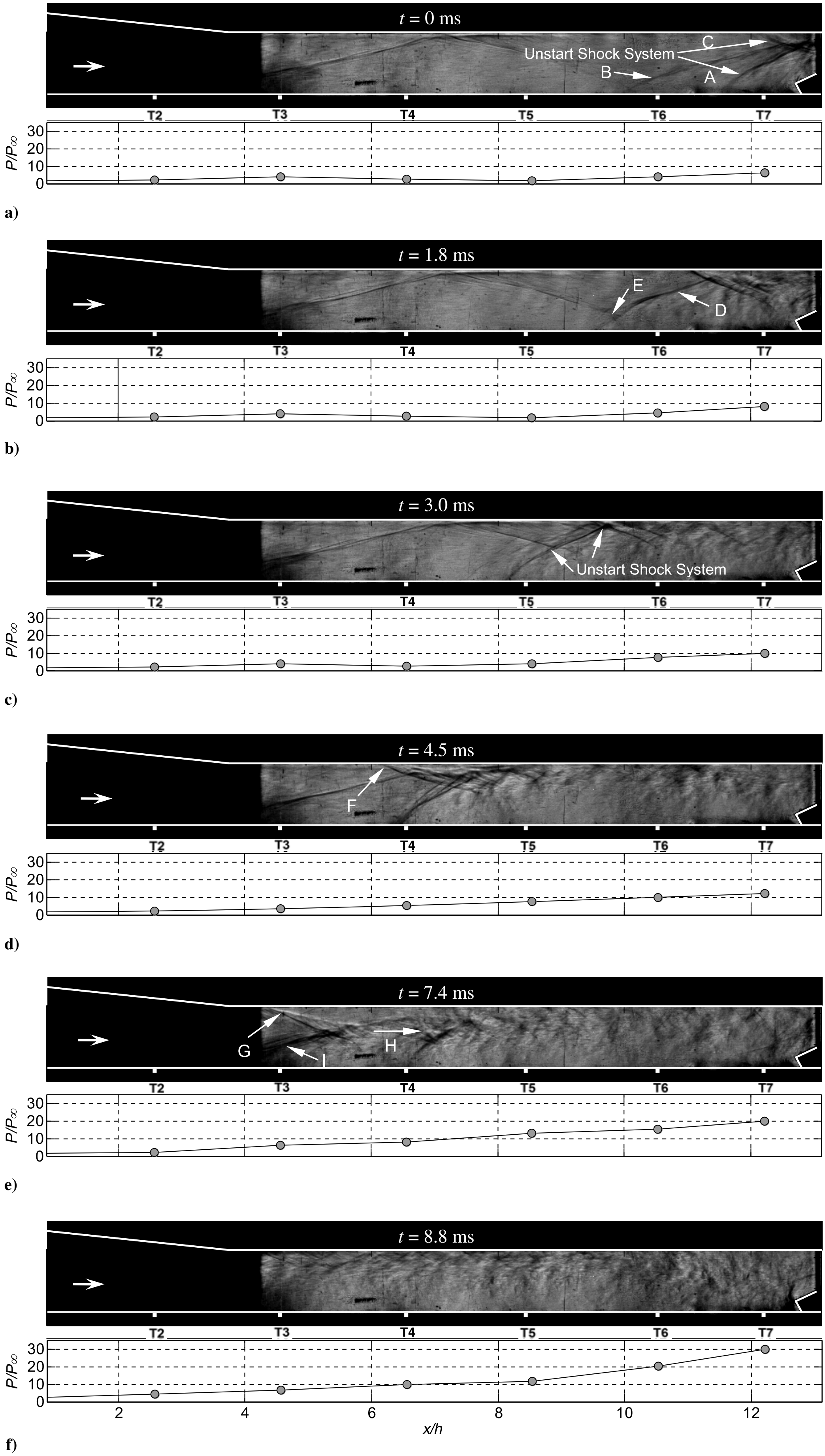

Fig. 9 Sequence of downstream-view schlieren images and corresponding instantaneous pressure distributions showing the unstart process: a) $t = 0$, b) $t = 1.8$, c) $t = 3.0$, d) $t = 4.5$, e) $t = 7.4$, and f) $t = 8.8$ ms.

velocity reported by Rodi et al. [18]. In comparison, the average unstart propagation velocity in the isolator (between T6 and T3) is much slower at $0.035 \pm 0.003\ U_\infty$ (26 ± 2 m/s). Wieting [17] reported a similar velocity of 27 m/s in a constant area section of a model scramjet. The average unstart propagation velocity through the entire inlet/isolator model is $0.05 \pm 0.003\ U_\infty$ (37 ± 2 m/s). The observed average velocity range in this experiment of 19–80 m/s is broader than those measured experimentally by Wieting [17] (10–27 m/s) or Rodi et al. [18] (55–70 m/s).

The flow structure of the unstart process as seen in the downstream view and with a vertical knife edge (which is sensitive to streamwise density gradients) is shown in Fig. 9. Six images and their corresponding pressure distributions at times of 0, 1.8, 3.0, 4.5, 7.4, and 8.8 ms are shown. The onset of unstart, seen at $t = 0$ ms (Fig. 9a), corresponds to the absolute time of 0.191 s in Fig. 6. Note that some of the observations made in this section were made with high-speed movies and may not be readily seen in the time sequences shown. Looking to the rear of the isolator at the onset of unstart, the flap shock (arrow A) and final reflected shock (arrow B) remain separate entities. These shocks interact at their impingement location on the isolator ceiling where the flow separates and another shock forms in response to this separated flow (arrow C). This separation shock, in combination with the flap shock, marks the unstart shock system (arrows A and C). As time progresses, the unstart shock system moves upstream and the flap shock appears to coalesce with the final reflected oblique shock. The unstart shock system is seen to be asymmetric with respect to the isolator horizontal centerline, probably owing to the thicker boundary layer on the floor as compared to the ceiling. As this shock system moves upstream, the pressure at T7 ($x/h = 12.21$) rises. In Fig. 9b at $t = 1.8$ ms, the lower upstream leg of the unstart shock system has now replaced what was initially the third reflected shock of the started flow (arrow D). During this process, the pressure at T6 ($x/h = 10.53$) rises in response to this stronger shock. Also, between 0 and 1.8 ms, the shock angle of the lower upstream leg of the unstart shock system increases near its intersection with the floor. In addition, this lower upstream leg becomes increasingly more bifurcated with unstart progression (arrow E), which indicates an increase in the degree of separation of the lower-wall boundary layer. Similar observations were made by Neaves et el. [23]. From $t = 1.8$–3.0 ms (Fig. 9c), the pressure at T5 ($x/h = 8.54$) increases as the unstart shock system moves upstream through the region initially containing the second reflected shock. Between 3.0 and 4.5 ms (Fig. 9d), the unstart shock system continues to move upstream and the pressure at T7–T5 continues to rise. At $t = 4.5$ ms, the presence of the unstart shock system has caused separation of the isolator ceiling boundary layer (arrow F). This separation was seen to begin at the impingement point of the first reflected shock of the initial oblique shock system. Also, the pressure has risen at T4 ($x/h = 6.56$) as the lower upstream leg of the unstart shock system has passed over it. Between 4.5 and 7.4 ms (Fig. 9e), the unstart shock system continues to propagate upstream with increasing separation of the ceiling boundary layer. The $t = 7.4$ ms image shows propagation of the unstart shock system has resulted in the formation of a prominent shear layer (arrows G and H) that originates at the separation point of the isolator ceiling boundary layer (arrow G). Figure 8b shows that the propagation velocity of the unstart shock system tends to slow down between $x/h = 6.56$ and 3.57. However, it should be noted that the unstart shock system velocity is determined by the pressures measured on the floor of the isolator. Therefore, this result only shows propagation along the floor of the isolator slows as the ceiling boundary layer separates. Another feature of the $t = 7.4$ ms image is the first reflected shock of the initial reflected oblique shock system has "lifted" slightly (arrow I). As a result, the pressure at T3 ($x/h = 4.57$) increases by about a factor of 2 over that at the previous time. Finally, at 8.8 ms (Fig. 9f), which corresponds to the absolute time of 0.20 s of Fig. 6, the unstart shock system has moved farther upstream into the converging inlet section and increases the pressure at T2 ($x/h = 2.58$). The pressures at T7–T3 have further increased and the resulting isolator flow is seen to be highly separated.

A time-sequence of upstream-view schlieren images is shown in Fig. 10. Eight images taken with a horizontal knife edge (to highlight vertical gradients) are shown for the times of 0, 2.9, 3.9, 7.6, 8.5, 9.3, 10.1, and 15.4 ms from the onset of unstart. In addition, the pressure time history of each transducer during this unstart event is given in Fig. 11. Because the upstream view does not show the onset of unstart, the pressure-determined onset of unstart is used. At $t = 0$ ms (Fig. 10a), the inlet/isolator is started. At 2.9 ms (Fig. 10b), the unstart shock system has moved upstream intersecting the floor between T5 and T4 at an approximate location of $x/h = 7.5$ (arrow A). As shown in Fig. 11, the pressure at T6 and T5 has risen with the passage of the unstart shock system. Looking to Fig. 10c at $t = 3.9$ ms, the unstart shock system is far enough upstream to induce significant boundary-layer separation on the ceiling of the isolator (arrow B). As demonstrated in the $t = 7.6$ ms image (Fig. 10d), as time progresses, the upper boundary layer separates further and the unstart shock system moves upstream with the upstream motion of the ceiling boundary-layer separation point (arrow C). At this time, the pressure at T4 and T3 has risen due to the passage of the unstart shock system. Also, the first reflected shock of the initial started flowfield appears to be lifted (arrow D) in response to the propagating unstart shock system. Neaves et el. [23] reported a similar lifting effect due to unstart. At $t = 8.5$ ms (Fig. 10e), the unstart shock system has propagated upstream of the inlet entrance (arrow E). However, the unstart shock system has not yet crossed over the T1 location. Figure 11 shows the pressure rise at T1, due to the crossing of the unstart shock system, occurs at about $t = 8.6$ ms. At $t = 9.3$ ms (Fig. 10f), the unstart shock system has crossed upstream over T1 (arrow F). A separated flow appears to be emanating from the ceiling (arrow G) and impinging on the isolator floor (arrow H). Up until 9.3 ms, the unstart shock system has undergone only upstream motion; however, from $t = 9.3$ to 10.1 ms (Fig. 10g), the leading shock (arrow I) of the unstart shock system moves downstream. Figure 11 shows that this results in a decrease in the T1 pressure to the preunstart level. The $t = 10.1$ ms image also shows that the floor impingement point of the separated flow has moved downstream (arrow J). As demonstrated in Fig. 11, the isolator pressure distribution (T7–T3) decreases with the downstream propagation of the unstart shock system. The pressure decrease is first seen at T3 ($t = 9.3$ ms), followed by T4 ($t = 9.5$ ms), T5 ($t = 9.9$ ms), T6 ($t = 10.7$ ms), and finally T7 ($t = 10.9$ ms). Similar pressure time histories were seen during each of the 10 unstart events of Fig. 8a. This indicates that the temporary downstream propagation of the unstart shock system described in this section is typical of the unstart process in the current model. It is possible that this downstream motion is part of an acoustic resonator oscillation. For instance, at $t = 9.3$ ms, the leading shock (arrow I) is most likely strong enough to induce significant separation and therefore some subsonic flow. With some subsonic flow entering the inlet entrance, it can now act as an open end for an acoustic resonator. Figure 11 shows that, following local minima, the pressures at T1–T7 increase, which was seen in the schlieren imaging (not shown here) to be associated with the unstart shock system reverting back to upstream propagation. It was also observed from the schlieren images that, after about 13 ms, the leading oblique shock of the unstart shock system no longer intersected the inlet ceiling. Rather, it had moved far enough upstream to be considered a bow shock that passes over the inlet. Without the impingement of the leading oblique shock on the inlet ceiling, there was no longer a separated flow emanating from the ceiling. With increasing time, the unstart bow shock continued to move upstream. Figure 11 shows that, as the bow shock moves upstream, the pressure within the model decreases rapidly ($t \approx 14$–17 ms) and becomes much more uniform, indicating the flow in the model is subsonic. The $t = 15.4$ ms image of Fig. 10h demonstrates this point. The unstart bow shock is out of the field of view and estimated to be near a maximum upstream location. The lack of waves and strong gradients within the entire visible portion of the isolator suggests the isolator flow is subsonic. Up until 17.25 ms, where the model pressure decreases to a minimum, the flowfield looks very similar to that of the $t = 15.4$ ms image. The fact that the pressure distribution decreases as the unstart bow shock moves

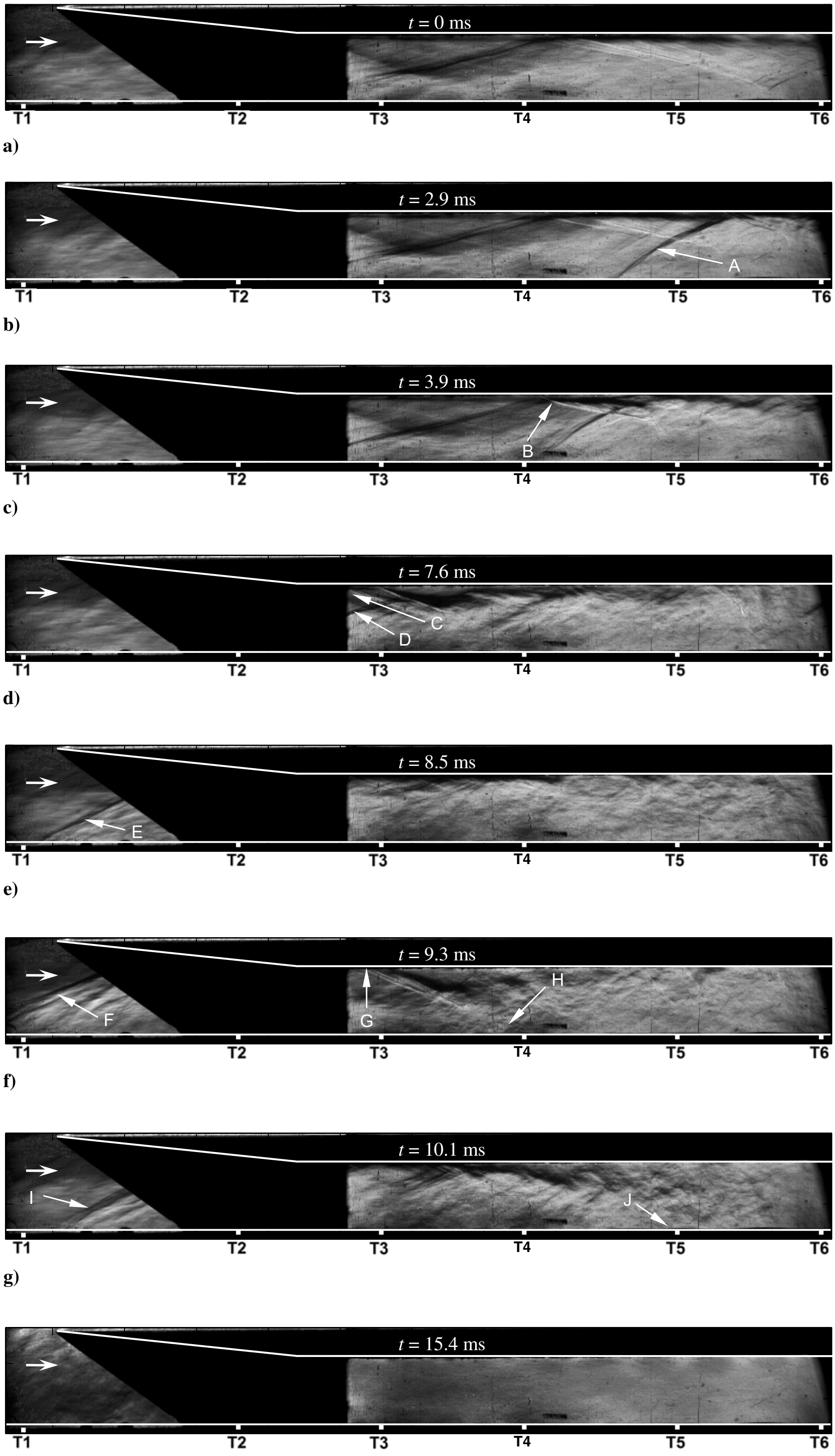

Fig. 10 Sequence of upstream-view schlieren images showing the unstart process: a) $t = 0$, b) $t = 2.9$, c) $t = 3.9$, d) $t = 7.6$, e) $t = 8.5$, f) $t = 9.3$, g) $t = 10.1$, and h) $t = 15.4$ ms.

upstream may be attributed to increased spillage over the top and around the sides of the inlet entrance.

F. High-Amplitude Oscillatory Unstarted Flow

Once the inlet/isolator model unstarted, high-amplitude periodic pressure fluctuations at T7 as high as 35 P_∞ occurred as seen in Fig. 3 from 0.19 to 0.45 s. A few cycles of these oscillations at T7 can be seen in Fig. 6. The previous section described the first pressure rise and fall during unstart. This section focuses on the pressure oscillations that follow unstart. Figure 12 is a series of representative downstream-view schlieren images and the corresponding wall-pressure distributions for this process. The knife edge was in a

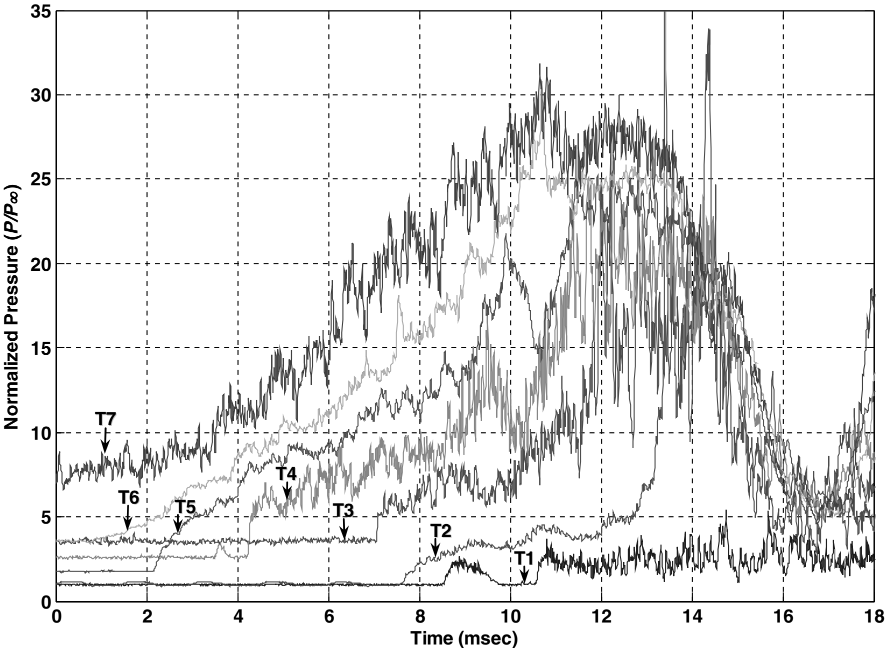

Fig. 11 Pressure time histories obtained at T1–T7 for the unstart event of Fig. 10.

vertical position to highlight horizontal gradients such as those due to normal shocks and compression waves. In this section, observations made of other high-amplitude oscillatory unstarted flow cycles using the upstream view will also be discussed. The first image in Fig. 12 corresponds to the absolute time of 0.31 s in Fig. 3, and the sequence is for the relative times of $\phi = 0$, 1.1, 2.6, 3.0, 3.9, and 4.3 ms, which represents part of a oscillation cycle. In this section, the time $\phi = 0$ ms is chosen to be when the overall isolator pressure distribution is at a near cycle maximum. In the $\phi = 0$ image of Fig. 12a, visible flow features are apparent near the isolator entrance (arrow A). The featureless flow in the downstream section of the isolator indicates that the flow is largely subsonic. Upstream-view schlieren images for other high-amplitude oscillatory unstarted flow cycles (not shown here) were used to determine the flow structure near the inlet entrance. The images indicated that, at cycle times when the isolator pressure distribution was at a near maximum (such as at $\phi = 0$ of Fig. 12a), an oblique shock sat upstream of the inlet floor and intersected the inlet ceiling just downstream of $x/h = 0$. The $\phi = 1.1$ ms image (Fig. 12b) shows that the flow within the entire isolator is quiescent and most likely subsonic. Upstream-view images of other cycles showed this quiescent flow to be the result of a bow shock that sat upstream of the inlet. The pressure distribution at $\phi = 1.1$ ms indicates the isolator pressure is lower than that at $\phi = 0$. During the decreasing-pressure part of the cycle, downstream-propagating compression waves were observed. These compression waves became more distinct in the schlieren images when the isolator pressure distribution was near a minimum. In Fig. 12c at $\phi = 2.6$ ms, the isolator pressure distribution has further decreased and a compression wave has propagated to near the downstream end of the isolator. The wave is seen as a vertical white line (arrow B) at the approximate streamwise location of $x/h = 11$. From the schlieren time sequence, the velocity of the compression wave was estimated to be about 350 m/s near the downstream section of the isolator. Similar compression wave velocities were observed in other high-amplitude oscillatory unstarted flow cycles. Another key feature of the $\phi = 2.6$ ms image is that the visible flow features (arrow C) have reentered the entrance of the isolator. Upstream-view images revealed that, as these visible flow features moved back within the isolator, the bow shock upstream of the inlet moved downstream to once again intersect the inlet ceiling as an oblique shock. The $\phi = 3.0$ ms image (Fig. 12d) shows an upstream-propagating strong bifurcated normal shock is near the exit of the isolator (arrow D). This normal shock appears to be related to the acoustic-compression waves that reflect off the flap at the end of the isolator. Also note, in the $\phi = 3.0$ ms image, that the visible flow features (arrow E) have moved even further downstream into the isolator. The upstream-view schlieren images showed that, as the visible flow features moved further downstream, the oblique shock upstream of the inlet also moved further downstream. As time progresses between $\phi = 3.0$ and 3.9 ms (Fig. 12e), the visible flow features at the isolator entrance continue to move downstream as the flow becomes supersonic, while the strong compression system generated at the exit of the isolator continues to move upstream. As a result, two distinct shock systems (arrows F and G) form within the isolator, as seen in the $\phi = 3.9$ ms image. The pressure in the downstream half of the isolator has increased as the strong shock generated at the rear of the isolator has moved upstream toward the center of the isolator. This upstream-propagating shock system can be seen at the streamwise location of about the $x/h = 8.5$ (arrow F), followed by highly separated flow. The downstream-propagating shock system can be seen near $x/h = 6$ (arrow G). This shock system is seen to be associated with a separated upper isolator boundary layer. As seen in the $\phi = 4.3$ ms image (Fig. 12f), the two shock systems interact and merge into a new single shock system (arrow H). Near the time of this merging, observations made with the upstream view (of other cycles) suggest that the oblique shock upstream of the inlet has reached a maximum downstream location close to floor of the inlet entrance. In subsequent images (not shown here), the shock system (of arrow H) then moves upstream until a near maximum pressure distribution is obtained in the inlet/isolator at about $\phi = 7.4$ ms. The flowfield image and pressure distribution at this time (not shown here) are very similar to those seen at $\phi = 0$. Referring to Fig. 6, it can be seen that the rise time to peak pressure is noticeably smaller for high-amplitude oscillatory cycles as compared to the initial unstart transient. This faster isolator pressurization compared to the initial unstart pressurization may be related to the upstream- and downstream-propagating compression waves observed in the high-amplitude oscillatory unstarted flow schlieren images.

Figure 13 shows the power spectra of transducers T7, T2, and T1 for the high-amplitude oscillatory unstarted flow. For all spectra presented in this paper, the acquisition rate was 192 kHz and the number of samples taken was 48,000, which gives a maximum frequency of 96 kHz and a resolution of 4 Hz. However, the frequency information is only valid up to the low-pass filter cutoff frequency of 50 kHz. Absolute frequencies as well as normalized frequencies are presented as follows. Unstarted-flow frequencies were normalized as $f^* = fL/a_0$ (where $a_0/L = 1100$ Hz), which would be appropriate for a purely acoustic oscillation.

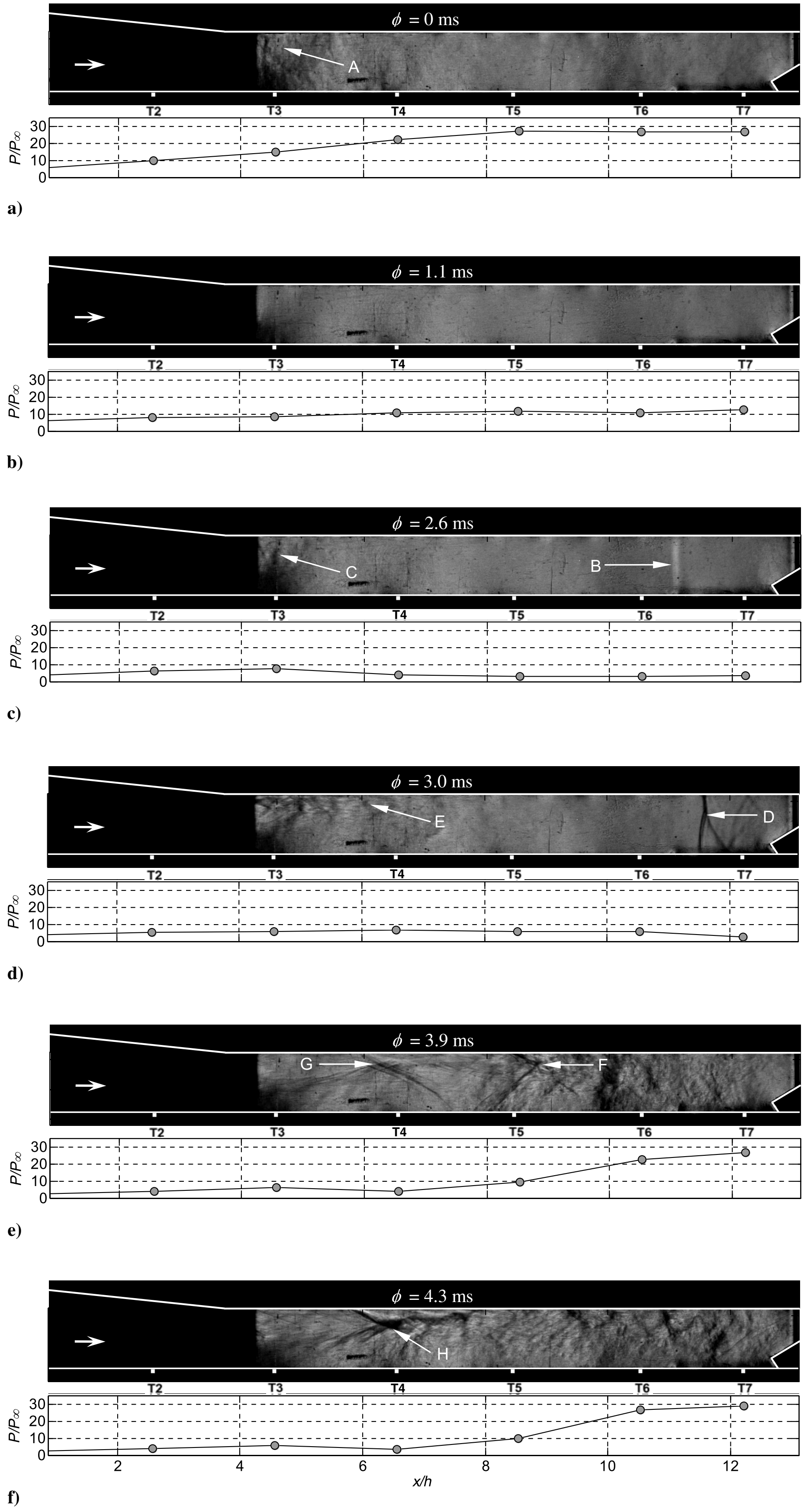

Fig. 12 Sequence of downstream-view schlieren images and corresponding instantaneous pressure distributions showing high-amplitude oscillatory unstarted flow: a) $\phi = 0$, b) $\phi = 1.1$, c) $\phi = 2.6$, d) $\phi = 3.0$, e) $\phi = 3.9$, and f) $\phi = 4.3$ ms.

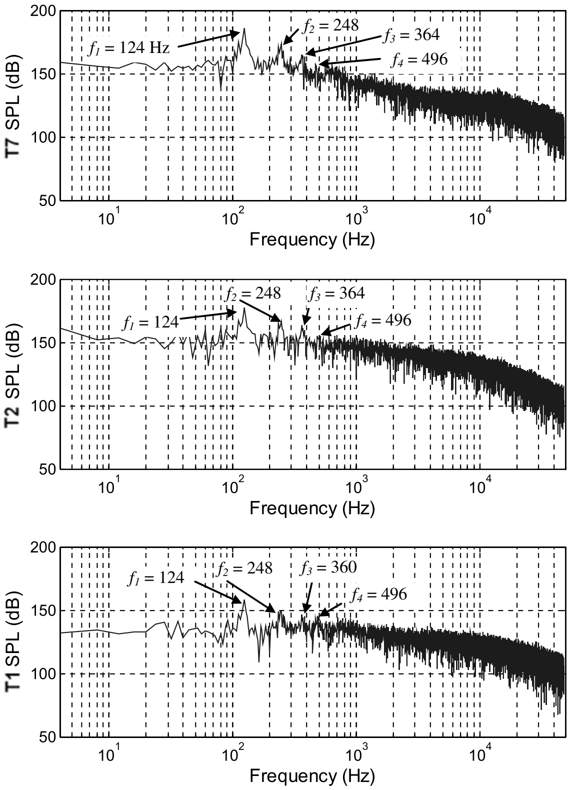

Fig. 13 Power spectra of the pressure at T7, T2, and T1 for the high-amplitude oscillatory unstarted flow.

For example, use of these parameters would yield normalized frequencies of $f^* = 0.25$ and 0.5 for quarter- and half-wave resonators, respectively. As seen in Fig. 13, the dominant frequency f_1 for T7, T2, and T1 is about 124 Hz ($f_1^* = 0.11$). The other four transducers also showed the same value of dominant frequency. The second and fourth highest peaks occur at the second and fourth harmonics of the dominant frequency ($f_2 = 248$ Hz, $f_2^* = 0.23$ and $f_4 = 496$ Hz, $f_4^* = 0.45$) and the third highest peaks occur near the third harmonic at about 364 Hz ($f_3^* = 0.33$). The spectra for T6–T3 (not shown here) within the isolator look very similar to that of T7, but the sound pressure levels (SPL) tend to decrease for the more upstream transducers. For example, the dominant peak occurs at 186 dB for T7 and 180 dB for T3. As seen in Fig. 13, the T2 (within the inlet) power spectrum looks similar to that of T7, but the dominant peak occurs at a lower SPL of 177 dB. The SPL distribution of T1 (upstream of the inlet) is seen to be much lower than those of T7–T2. Such oscillatory unstarted flow pressure distributions have also been observed by other researchers [18–20]. Rodi et al. [18] found the frequency of their oscillatory unstarted flow could be predicted by using linear acoustic theory for a half-wave resonator (i.e., the inlet/isolator is a resonator with two free boundaries). The speed of sound was calculated using the flow stagnation temperature. If in the current study we do the same, the calculation gives an oscillation frequency of 550 Hz ($f^* = 0.5$), which is more than 4 times the observed dominant frequency. As previously mentioned, because the traveling shocks can be clearly seen to reflect as shocks, this means that the isolator exit acts more like a solid wall, and so treating the isolator as a quarter-wave resonator may be more appropriate. Doing so gives a resonant frequency of 275 Hz ($f^* = 0.25$), which is still more than twice the measured frequency. There do appear to be times in the oscillatory cycle for which acoustic theory may be appropriate. For instance, the compression wave of Fig. 12c at $\phi = 2.6$ ms propagates at a velocity of about 350 m/s which is near the stagnation speed of sound. However, there are other times in the oscillatory cycle where it is rather obvious that linear acoustic theory should not apply. For example, the Fig. 12 images at $\phi = 3.9$ and 4.3 ms show the isolator flow to be dominated by strong propagating shock systems (arrows F and G) that are associated with flow separation. In Fig. 12d at $\phi = 3.0$ ms, the upstream-propagating shock system (arrow D) is at the location of about $x/h = 11.5$. At $\phi = 3.9$ ms (Fig. 12e), the shock system (arrow F) has moved upstream to the approximate location of $x/h = 8$. Using the difference in approximate locations of the upstream-propagating shock system between the $\phi = 3.0$ ms image and the $\phi = 3.9$ ms image gives a rough shock system velocity estimate of 100 m/s. This lower-than-acoustic velocity is likely because the upstream-propagating shock system propagates against a supersonic flow. Owing to cycle times for which the isolator flow is dominated by propagating shock systems, frequencies lower than that predicted by linear acoustic theory are to be expected.

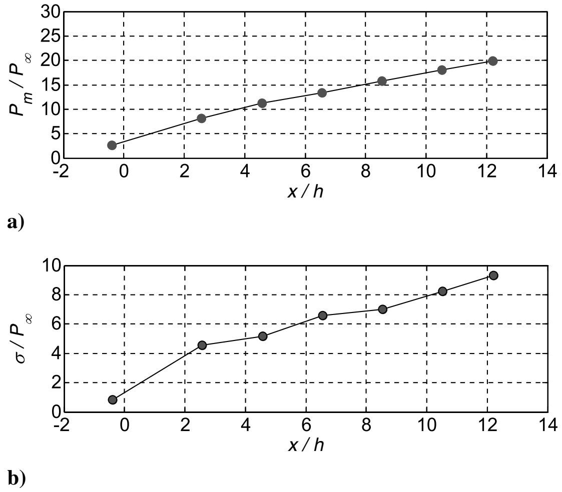

Fig. 14 High-amplitude oscillatory unstarted flow: a) mean pressure distribution, and b) pressure standard deviation distribution.

The mean pressure and rms pressure distributions for the high-amplitude oscillatory unstarted flow are shown in Fig. 14. Both distributions are seen to increase in a nearly linear fashion with streamwise distance into the inlet/isolator model. Compared with the fully supersonic started flow of Fig. 5, this unstarted flow is seen to have much higher rms and mean pressures.

G. Nonoscillatory Unstarted Flow

As seen in Fig. 3, at a time of about 0.5 s, the flap was brought to a slightly lower position, maintaining an unstarted inlet/isolator. However, this unstarted flow had much smaller pressure fluctuations at T7 (about 10 P_∞). The pressure power spectra at each transducer during this time reveal that the fluctuations are more broadband and

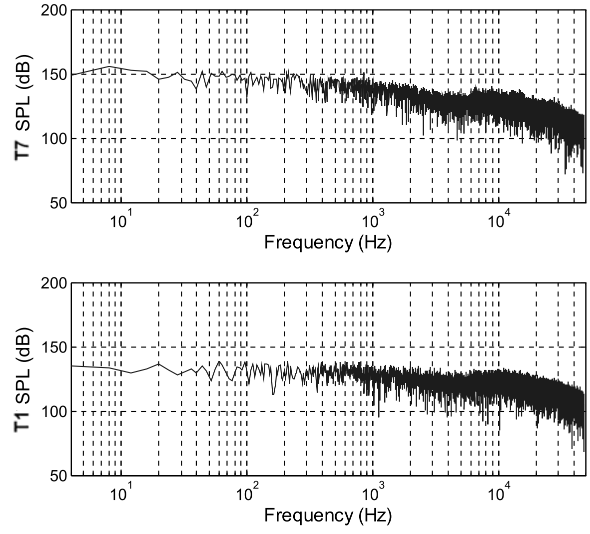

Fig. 15 Power spectra of the pressure at T7 and T1 for nonoscillatory unstarted flow.

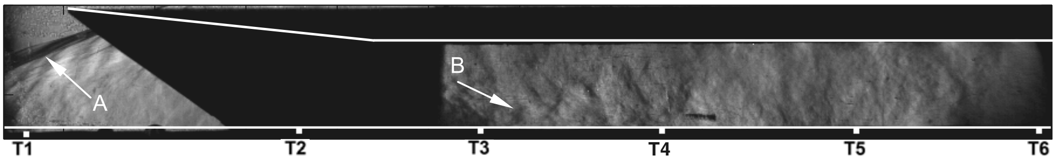

Fig. 16 Upstream-view schlieren image showing nonoscillatory unstarted flow.

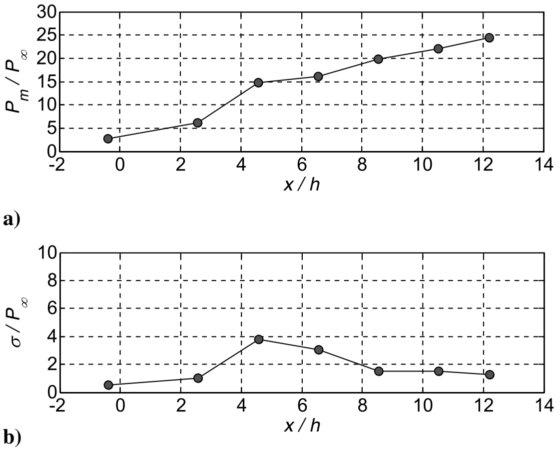

Fig. 17 Nonoscillatory unstarted flow: a) mean pressure distribution, and b) pressure standard deviation distribution.

do not exhibit the dominant peaks seen in the oscillatory unstarted flow described earlier. For example, the pressure power spectra for T7 and T1 are shown in Fig. 15 and demonstrate the broadband nature of the fluctuations. Furthermore, compared to the high-amplitude oscillatory unstarted flow, the nonoscillatory unstarted flow is seen to have lower SPL levels. An example of an upstream-view schlieren image from the nonoscillatory unstarted flow is shown in Fig. 16. This image was taken from another nonoscillatory unstarted flow similar to that shown in Fig. 3. During this unstarted flow mode, an oblique shock (arrow A) is always seen to sit upstream of the inlet entrance. A shear layer (arrow B) that appears to be the result of ceiling boundary-layer separation is also always seen during this mode. The mean pressure distribution plot of Fig. 17a shows the mean pressure near the end of the isolator (at T7) to be 23.9 P_∞, which is 86% of the pressure computed for a Mach 4.9 normal shock of 27.8 P_∞. Furthermore, Fig. 17b shows that the pressures of this unstarted flow mode are much steadier than that for the high-amplitude oscillatory unstarted flow (compare to Fig. 14b).

H. Lower-Amplitude Oscillatory Unstarted Flow

As shown in Fig. 3, at a time of about 1.0 s, the flap was slightly raised resulting in what is termed lower-amplitude oscillatory unstarted flow. The T7 pressure fluctuations of about 20 P_∞ that occur from about 1.0 to 1.3 s are lower than those observed during the high-amplitude oscillatory unstarted flow. Observations of downstream-view schlieren images (not shown here) appear to show downstream- and upstream-propagating compression waves. However, compared to the high-amplitude oscillatory unstarted flow, these waves appear much less frequently in the schlieren images. In addition, the waves are far less pronounced, indicating they are weaker than in the high-amplitude case. Figure 18 shows the power spectra for T7, T2, and T1 for this unstarted flow mode. The highest peak and second highest peaks are seen to occur at $f_1 = 84$ Hz ($f_1^* = 0.076$) and $f_2 = 68$ Hz ($f_2^* = 0.062$) for both T7 and T2. To summarize, Table 1 gives the dominant frequencies for T7 and the corresponding SPL values for both oscillatory unstarted flow modes.

For the lower-amplitude flow, the same frequency values were seen to correspond to the highest and second highest peaks for the spectra of T6-T3 (not shown here) as well. The spectra for T6–T3 are similar to that of T7, but the SPL level decreases for upstream transducers. For example, the highest peak SPL value is 174 dB for T7 and 164 dB for T3. As seen in Fig. 18, the T2 SPL peak of 173 dB is close to that of T7. (This was not the case in the high-amplitude oscillatory unstarted flow for which the T2 SPL peak was lower than those of T7–T3.) T1 has a peak SPL value at $f_1 = 16$ Hz ($f_1^* = 0.015$). The second and third highest peaks occur at $f_2 = 84$ Hz ($f_2^* = 0.076$) and $f_3 = 68$ Hz ($f_3^* = 0.062$). The mean pressure and rms pressure distributions for this flow are shown in Fig. 19. The mean isolator pressure distribution for the lower-amplitude unstarted flow is higher than that of the high-amplitude case shown in Fig. 14. The mean rms pressure distribution exhibits a maximum at T2 located just inside the inlet portion of the model. This indicates that streamwise oscillations of the unstarted shock system occur close to T2 near the inlet entrance.

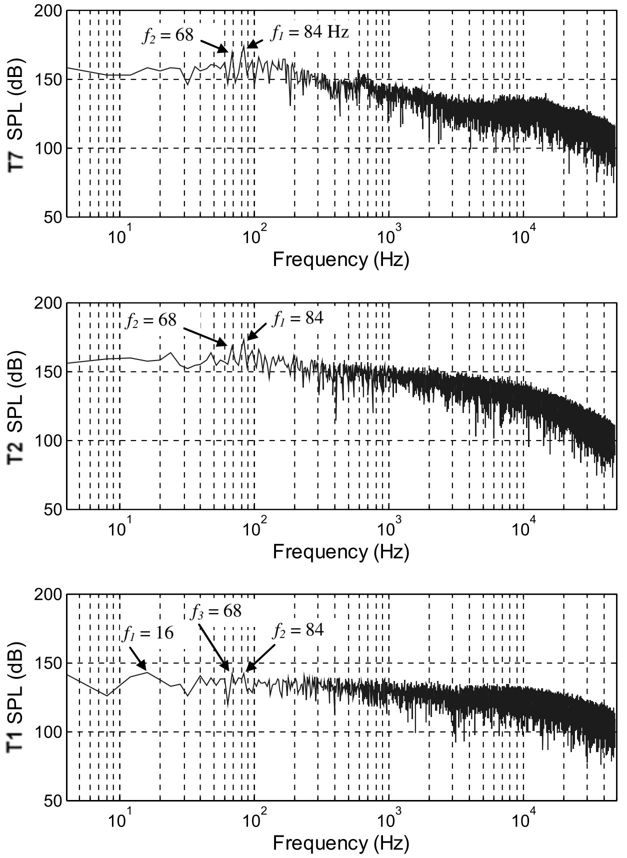

Fig. 18 Power spectra of the pressure at T7, T2, and T1 for the lower-amplitude oscillatory unstarted flow.

Table 1 Dominant Frequencies and SPL for Oscillatory Unstarted Flows at Transducer T7

Amplitude	f_1, Hz	f_1^*, normalized	SPL, dB
High	124	0.11	186
Lower	84	0.076	174

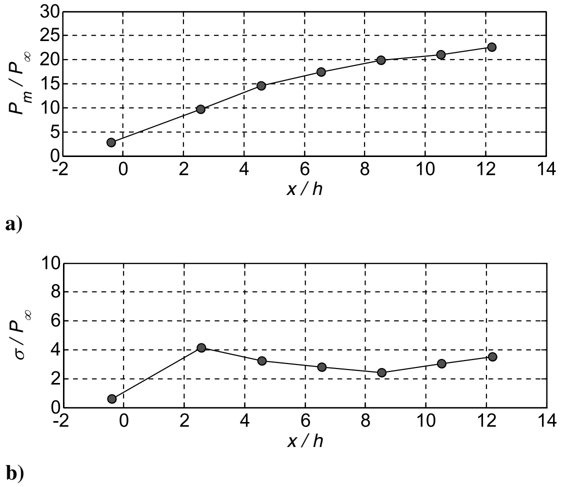

Fig. 19 Lower-amplitude oscillatory unstarted flow: a) mean pressure distribution, and b) pressure standard deviation distribution.

IV. Conclusions

Unstart dynamics were investigated experimentally in an inlet/isolator model mounted on the floor of a Mach 5 wind tunnel. The model consisted of an inlet with a 6-deg compression ramp followed by a rectangular isolator that was 25.4-mm high by 50.8-mm wide by 242.3-mm long. The incoming boundary-layer thickness was about 19 mm, which was a large fraction of the inlet height of 34.9 mm. Unstart was initiated by raising a flap at the exit plane of the isolator. Varying the flap rise time did not show any discernible effects with regard to unstart time scales or unstart flow structure. Near the unstart condition, a rapid increase in boundary-layer separation was observed near the isolator exit owing to the interaction of the reflected inlet shock and flap shock on the ceiling of the isolator. Upstream propagation of the unstart shock system was seen to be highly associated with shock-induced separation. The average velocity of unstart propagation in the constant area isolator section was about 0.035 U_∞ (26 m/s), whereas the average velocity of unstart for the inlet was about 0.10 U_∞ (74 m/s). The average propagation velocity of the unstart shock system through the entire inlet/isolator was about 0.05 U_∞ (37 m/s).

Once the inlet unstarted, a highly oscillatory unstarted flow was seen to form with a frequency of about 124 Hz or 0.11 a_0/L. Simultaneous imaging and pressure measurements showed the mechanism for these oscillations to be related to downstream-propagating compression waves that reflect off the end of the isolator exit. The pressure increase during the high-amplitude oscillatory unstarted flow mode occurred in less time than the initial pressure rise that characterizes the initial unstart event. This observation is likely related to the fact that pressurization during unstart appeared to be highly dependent on flow separation, whereas pressurization during the oscillatory unstarted flow was seen to be partly dependent on downstream-propagating compression waves at near-acoustic velocities.

Two other unstarted flows were seen to occur, including a second mode of oscillatory unstarted flow with a frequency of about 84 Hz or 0.076 a_0/L and lower pressure fluctuations than the high-amplitude case. Also, a nonoscillatory unstarted flow has been studied. This nonoscillatory unstarted flow was seen to always contain an oblique shock upstream of the inlet entrance and a shear layer apparently owing to separation of the model's ceiling boundary layer. The nonoscillatory unstarted flow had lower pressure fluctuations than the oscillatory unstarted flows.

Acknowledgments

The research work was supported by the U.S. Air Force Office of Scientific Research under Multidisciplinary University Research Initiative grant FA9550-04-1-0387. The authors gratefully acknowledge this source of support. The authors would like to thank B. Ganapathisubramani for his help during the preliminary phases of the experiment and Edward Zihlman for his help during data acquisition.

References

[1] Curran, E. T., and Stull, F. E., "The Utilization of Supersonic Combustion Ramjet Systems at Low Mach Numbers," Aero Propulsion Lab., RTD-TDR-63-4097, Jan. 1964.

[2] Curran, E. T., Heiser, W. H., and Pratt, D. T., "Fluid Phenomena in Scramjet Combustion Systems," *Annual Review of Fluid Mechanics*, Vol. 28, Jan. 1996, pp. 323–360.
doi:10.1146/annurev.fl.28.010196.001543

[3] Heiser, W. H., and Pratt, D. T., *Hypersonic Air Breathing Propulsion*, AIAA Education Series, AIAA, Washington, D.C., 1993.

[4] Emami, S., Trexler, C. A., Auslender, A. H., and Weidner, J. P., "Experimental Investigation of Inlet-Combustor Isolators for a Dual Mode Scramjet at a Mach Number of 4," NASA TP-3502, May 1995.

[5] Wang, C.-P., Zhang, K.-Y., and Cheng, K.-M., "Pressure Distribution Measurements in Scramjet Isolators Under Asymmetric Supersonic Flow," AIAA Paper 2006-818, Jan. 2006.

[6] Bachchan, N., and Hillier, R., "Effects of Hypersonic Inlet Flow Non-Uniformities on Stabilising Isolator Shock Systems," AIAA Paper 2004-4716, Aug. 2004.

[7] Matsuo, K., Miyazato, Y., and Kim, H.-D., "Shock Train and Pseudo-Shock Phenomena in Internal Gas Flows," *Progress in Aerospace Sciences*, Vol. 35, No. 1, 1999, pp. 33–100.
doi:10.1016/S0376-0421(98)00011-6

[8] Waltrup, P. J., and Billig, F. S., "Structure of Shock Waves in Cylindrical Ducts," *AIAA Journal*, Vol. 11, No. 10, 1973, pp. 1404–1408.
doi:10.2514/3.50600

[9] Waltrup, P. J., and Billig, F. S., "Prediction of Precombustion Wall Pressure Distributions in Scramjet Engines," *Journal of Spacecraft and Rockets*, Vol. 10, No. 9, 1973, pp. 620–622.
doi:10.2514/3.27782

[10] Reinartz, B. U., Herrmann, C. D., and Ballmann, J. B., "Aerodynamic Performance Analysis of a Hypersonic Inlet Isolator Using Computation and Experiment," *Journal of Propulsion and Power*, Vol. 19, No. 5, 2003, pp. 868–875.
doi:10.2514/2.6177

[11] Sullins, G., and McLafferty, G., "Experimental Results of Shock Trains in Rectangular Ducts," AIAA Paper 92-5104, Dec. 1992.

[12] Tam, C.-J., Lin, K-C., Davis, D. L., and Behdadnia, R., "Numerical Investigations on Simple Variable Geometry for Improving Scramjet Isolator Performance," AIAA Paper 2006-4509, July 2006.

[13] Stouffer, S. K., and Hagenmaier, M. A., "The Effect of Aspect Ratio on Isolator Performance," AIAA Paper 2001-0519, Jan. 2001.

[14] Hudgens, J. A., and Trexler, C. A., "Operating Characteristics at Mach 4 of an Inlet Having Forward-Swept Sidewall-Compression Surfaces," AIAA Paper 92-3101, July 1991.

[15] Masuya, G., Komuro, T., Murakami, A., Shinozaki, N., Nakamura, A., and Murayama, O., "Ignition and Combustion Performance of Scramjet Combustors with Fuel Injection Struts," *Journal of Propulsion and Power*, Vol. 11, No. 2, 1995, pp. 301–307.
doi:10.2514/3.51425

[16] Van Wie, D. M., Kwok, F. T., and Walsh, R. F., "Starting Characteristics of Supersonic Inlets," AIAA Paper 96-2914, July 1996.

[17] Wieting, A. R., "Exploratory Study of Transient Unstart Phenomena in a Three-Dimensional Fixed-Geometry Scramjet Engine," NASA TN D-8156, March 1976.

[18] Rodi, P. E., Emami, S., and Trexler, C. A., "Unsteady Pressure Behavior in a Ramjet/Scramjet Inlet," *Journal of Propulsion and Power*, Vol. 12, No. 3, 1996, pp. 486–493.
doi:10.2514/3.24061

[19] Shimura, T., Mitani, T., Sakuranaka, N., and Izumikawa, M., "Load Oscillations Caused by Unstart of Hypersonic Wind Tunnels and Engines," *Journal of Propulsion and Power*, Vol. 14, No. 3, 1998, pp. 348–353.
doi:10.2514/2.5287

[20] Hawkins, W. R., and Marquart, E. J., "Two-Dimensional Generic Inlet Unstart Detection at Mach 2.5–5.0," AIAA Paper 95-6016, April 1995.

[21] O'Byrne, S., Doolan, M., Olsen, S. R., and Houwing, A. F. P., "Analysis of Transient Thermal Choking Processes in a Model Scramjet Engine," *Journal of Propulsion and Power*, Vol. 16, No. 5, 2000, pp. 808–814.
doi:10.2514/2.5645

[22] Sato, T., and Kaji, S., "Study on Steady and Unsteady Unstart Phenomena Due to Compound Choking and/or Fluctuations in Combustor of Scramjet Engines," AIAA Paper 92-5102, Dec. 1992.

[23] Neaves, M. D., McRae, S., and Edwards, J. R., "High-Speed Inlet Unstart Calculations Using an Implicit Solution Adaptive Mesh Algorithm," AIAA Paper 2001-0825, Jan. 2001.

[24] McDaniel, K. S., and Edwards, J. R., "Simulation of Thermal Choking in a Model Scramjet Combustor," AIAA Paper 99-3411, June 1999.

[25] McDaniel, K. S., and Edwards, J. R., "Three-Dimensional Simulation of Thermal Choking in a Model Scramjet Combustor," AIAA Paper 2001-0382, Jan. 2001.

[26] Korkegi, R. H., "Comparison of Shock-Induced Two- and Three-Dimensional Incipient Turbulent Separation," *AIAA Journal*, Vol. 13, No. 4, 1975, pp. 534, 535.

N. Chokani
Associate Editor